Enabling IoT Self-Localization Using Ambient 5G Signals

Suraj Jog, Junfeng Guan, and Sohrab Madani, *University of Illinois at Urbana Champaign;* Ruochen Lu, *University of Texas at Austin;* Songbin Gong, Deepak Vasisht, and Haitham Hassanieh, *University of Illinois at Urbana Champaign*

https://www.usenix.org/conference/nsdi22/presentation/jog

This paper is included in the Proceedings of the 19th USENIX Symposium on Networked Systems Design and Implementation.

April 4–6, 2022 • Renton, WA, USA

978-1-939133-27-4

Open access to the Proceedings of the 19th USENIX Symposium on Networked Systems Design and Implementation is sponsored by

جامعة الملك عبدالله للعلوم والتقنية

King Abdullah University of Science and Technology

Enabling IoT Self-Localization Using Ambient 5G Signals

Suraj Jog[†], Junfeng Guan[†], Sohrab Madani[†], Ruochen Lu[⋆], Songbin Gong[†], Deepak Vasisht[†], Haitham Hassanieh[†]
University of Illinois at Urbana Champaign[†], *University of Texas at Austin*[⋆]

Abstract – This paper presents *ISLA*, a system that enables low power IoT nodes to self-localize using ambient 5G signals without any coordination with the base stations. *ISLA* operates by simply overhearing transmitted 5G packets and leverages the large bandwidth used in 5G to compute high-resolution time of flight of the signals. Capturing large 5G bandwidth consumes a lot of power. To address this, *ISLA* leverages recent advances in MEMS acoustic resonators to design a RF filter that can stretch the effective localization bandwidth to 100 MHz while using 6.25 MHz receivers, improving ranging resolution by 16×. We implement and evaluate *ISLA* in three large outdoors testbeds and show high localization accuracy that is comparable with having the full 100 MHz bandwidth.

1 Introduction

Recent years have witnessed a tremendous growth in the number of connected IoT devices, with surveys projecting up to 31 billion deployed IoT nodes by 2030 [38]. With such ubiquitous deployment of IoT nodes, the ability to localize and track these nodes with high accuracy is essential for many applications. For example, in data driven agriculture, it can enable real time micro-climate monitoring and livestock tracking [39]. In smart cities, IoT sensors are deployed throughout the city for tasks such as air quality monitoring, tracking buses, trains, and cars, and monitoring the structural health of infrastructure [22]. In the era of Industry 4.0, it can also enable wide area inventory tracking and facilitate factory automation [24].

Today, the most prevalent outdoors localization technology is GPS which is mainly used in cars and mobile phones. However, off-the-self GPS chips can consume about the same power as the entire IoT device, thus reducing the battery life to half in addition to the extra hardware costs [5]. Due to this, past work has proposed the use of cellular networks or dedicated IoT base stations for localization [9, 27]. These solutions, however, either achieve very low resolution of 100s of meters [9, 18] or require active participation of the base stations to jointly compute the location or tightly synchronize the base stations [27,40,45]. Realizing such solutions in practice requires the cooperation of cellular providers to bear the additional cost of modifying the base stations and a back end server to support the localization feature.

In this paper, *we ask whether an IoT device can accurately localize itself simply by listening to ambient 5G cellular signals, without any coordination with the 5G base stations?* Doing so would allow us to easily deploy self-localizing IoT nodes is wide areas without the need to modify the cellular base stations or deploy new base stations for localization.

5G cellular networks present unique opportunities for enabling accurate localization. First, the small cell architecture in 5G networks will lead to a very high density of 5G base stations, with up to 40 to 50 base stations deployed per square km [15], thereby allowing us to leverage more anchor points in the network for increased localization accuracy. Second, the 5G standard is designed to support very high data rates and can have OFDM signals spanning up to 100 MHz in bandwidth in the sub-6 GHz frequency range, and up to 400 MHz bandwidth in the mmWave frequency range [37]. Such large bandwidth can be used for accurate localization. To see how, consider the 5G OFDM signal shown in Fig. 1(a) where data bits are encoded in N frequency subcarriers. We can use the preamble which contains known bits to compute the channel impulse response (CIR) by taking an inverse FFT. The CIR in Fig. 1(a) shows the Time-of-Flight (ToF) of different signal paths. Estimating the ToF from few base stations allows us to localize the device. The larger the bandwidth of the signal, the higher the resolution. In fact, we can achieve a resolution of 3 meters for 100 MHz and 0.75 meters for 400 MHz signals.[1]

Leveraging these opportunities, however, is challenging since power-constrained and low-cost IoT nodes cannot capture the large bandwidth of the 5G signals. They are equipped with low-power and low-speed Analog-to-Digital Converters (ADCs) that can only capture a narrow bandwidth. In fact, while IoT has been one of the cornerstone applications in the design of 5G, it is only supported in narrowband chunks for low data rate applications [2, 3]. Therefore, while the 5G standard does allocate higher bandwidth (up to 400 MHz) for mobile broadband and high data rate applications, IoT nodes can capture only a very small fraction of this bandwidth ($\sim 20\times$ smaller [37]). As a result, they significantly lose out on the ToF resolution that was made possible by the high bandwidth 5G signals as shown in Fig. 1(b). Moreover, it is infeasible to measure the absolute time-of-flight without any coordination or synchronization with the base stations.

In this paper, we present *ISLA*, a system that enables **I**oT **S**elf-**L**ocalization using **A**mbient 5G signals. *ISLA* does not require any coordination with or modifications to the base stations. The key enabler of *ISLA* is the use of MEMS (micro-electro-mechanical-system) acoustic resonators. Past work [11, 12] has demonstrated that we can use such MEMS resonators to design new kinds of RF filters that look like a spike-train in the frequency domain, as shown in Fig. 1(c). To understand how we can leverage such MEMS spike-train filters, consider the 5G OFDM signal shown in Fig. 1(a).

[1] The resolution is computed as c/B where c is the speed of light and B is the bandwidth of the signal.

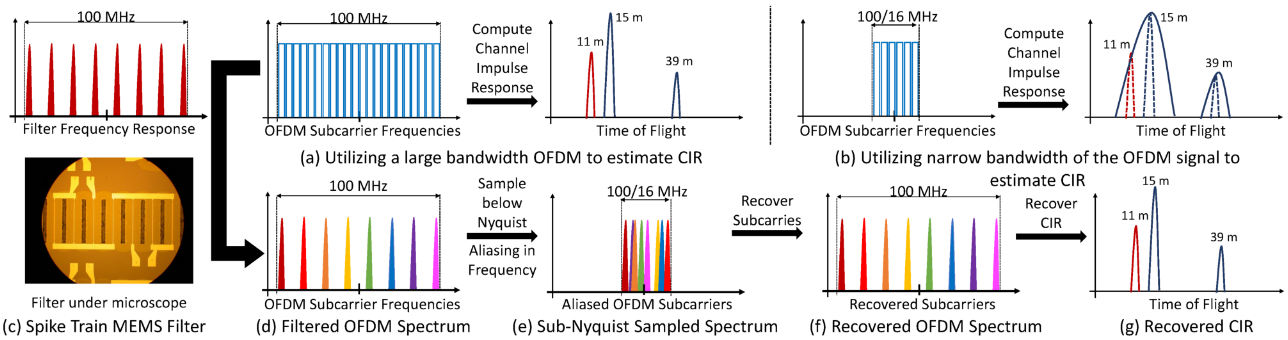

Figure 1: *ISLA*'s pipeline. (a) wideband OFDM signal and its corresponding CIR. (b) narrowband OFDM signal and its corresponding lower resolution CIR. (c) *ISLA*'s spike train MEMS filter that sparsifies the wideband signal. (d-f) follow the signal journey through *ISLA*'s pipeline that recovers the original CIR.

Passing this signal through the filter allows us to keep a few subcarriers of the wideband OFDM symbol while suppressing all other subcarriers as shown in Fig. 1(d). There are two important features of the resulting signal: (1) Since the remaining subcarriers that are passed by the filter span the entire wideband, we should, in principle, be able to recover the channel impulse response at the same high resolution of the original signal. (2) Since the remaining subcarriers create a sparse signal in the frequency domain, it should be possible to recover these subcarriers by sampling the signal below the Nyquist sampling rate using the same low-power low-speed ADCs on the IoT nodes.[2]

However, recovering the channel impulse response from a signal sampled with the low-speed ADCs is non-trivial. First, sampling the signal below the Nyquist rate leads to aliasing in the frequency domain as shown in Fig. 1(e). Some subcarriers might collide by aliasing on top of each other making it hard to recover these subcarriers. Past work in sparse recovery addresses this problem by using two co-prime subsampling rates [16]. Unfortunately, we do not have the flexibility to choose co-prime subsampling factors. In fact, since the number of OFDM subcarriers in the 5G standard is a power of 2 (e.g. 1024, 2048, 4096), we can only subsample the signal by powers of 2 otherwise the values of the subcarriers will be corrupted as we prove in section 5.[3] To address this, we carefully co-design the MEMS hardware with the recovery algorithm. In particular, we jointly optimize the filter shape (spacing between peaks, width of each peak, frequency span) with the subsampling rate to minimize the number of colliding OFDM subcarriers as we describe in detail in section 5.

Second, the recovered OFDM subcarriers are not uniformly distributed across the wideband bandwidth. This is because non-idealities in the MEMS filter make it hard to design a uniform spike train like the one shown in Fig. 1(c). As a result, we can no longer recover the CIR using standard super-resolution algorithms like MUSIC with spatial smoothing [21, 44] as they require uniform measurements. Instead, we formulate an inverse optimization problem that accounts for non-idealities and optimizes the CIR in the continuous time domain to achieve super resolution as described in Sec. 5.

Finally, while the above can provide very precise ToF measurements, these ToF estimates are not going to capture the true time taken by the signal to travel between the base station and the IoT device. This is because the 5G base stations are not time-synchronized with each other or the IoT device. To localize the device without any synchronization with the base station, *ISLA* leverages a second antenna on the receiver to compute the differential ToF of the propagation paths. While the absolute ToF measurements are corrupted by synchronization offsets, these offsets are constant across the 2 antennas on the IoT node, and hence can be eliminated by subtracting the measurements from the 2 antennas. Using this differential ToF at the IoT receiver, we show in section 7 that with measurements from four or more base stations, the IoT device can localize itself regardless of its orientation. We integrate our approach into a full system that addresses additional system challenges such as figuring the base station ID and accounting for carrier frequency offsets.

Evaluation: We implemented and evaluated *ISLA* indoors for microbenchmarks and outdoors for overall localization performance. We ran experiments in three outdoor settings:(1) Between campus buildings (52 m$\times$85 m), (2) a large parking lot (240 m$\times$400 m), and (3) an agricultural farm (480 m$\times$860 m). We use USRP X310 radios as base stations that can transmit high-bandwidth packets of 100 MHz. Our custom IoT nodes are equipped with 2 antennas and subsample the 5G signals at 6.25 MS/s which is 16$\times$ below the Nyquist rate. We fabricated a MEMS spike-train filter operating at a center frequency of 400 MHz and used it to demonstrate accurate reconstruction of the channel impulse response. However, due to significant interference at the 400 MHz band outdoors in our city, we ran experiments at 1 GHz and applied the filter response in digital. Our results reveal that with 5 base stations in range, *ISLA* can achieve a median accuracy of 1.58 m on campus, 17.6 m in the parking lot, and 37.8 m in the farm where the IoT node can be as much as 500 meters away from most base stations. For the parking lot testbed, the accuracy improves to 9.27 m with 15 base stations and 4.26 m with 25 base stations in range. We compare *ISLA*'s localization

[2]Note that the MEMS filter is passive and does not consume any power.

[3]For example, for a 100 MHz OFDM signal, we can only sample at 50 MS/s (2$\times$), 25 MS/s (4$\times$), 12.5 MS/s (8$\times$), 6.25 MS/s (16$\times$), ...

approach with several baselines [9, 21, 43] and show up to $4-11\times$ higher localization accuracy. Finally, we show that *ISLA* achieves a comparable performance to having a full 100 MHz receiver while using a $16\times$ lower sampling rate.

Contributions: We make the following contributions:

- We present, to the best of our knowledge, the first system that allows IoT nodes to localize themselves using ambient 5G signals without any coordination with the base stations.
- We demonstrate the ability to reduce the sampling rate by $16\times$ while retaining the benefits of high bandwidth 5G signals by leveraging recent advances in MEMS RF filters.
- We implement and evaluate *ISLA* to demonstrate accurate localization in 3 outdoor settings.

2 Related Work

Localization has been extensively studied in cellular, WiFi, and IoT networks. Our work differs from past research in that it is the first to enable self-localization using ambient 5G signals without requiring coordination with the base stations.

A. Cellular Based Localization: Several studies [9, 17, 18, 29, 33] have proposed to use nearby cell tower information and statistics in order to localize a mobile device. These methods, however, have a median accuracy of around 100 to 500 meters, and are mostly useful for very coarse localization. To improve localization accuracy, [4, 35] propose to combine WiFi APs with cellular base stations. Despite their relatively higher accuracy, these methods require fingerprinting the surroundings and as such require extensive training and do not generalize to new locations. More recent work exploits massive MIMO and millimeter wave for localization in 5G [30, 31, 42]. However, all of this work requires coordination with base stations and assumes the devices can capture the entire bandwidth of the 5G signals which does not work for IoT devices.

B. IoT Based Localization: [5] leverages TV whitespaces to achieve high localization accuracy for LoRA IoT devices. However, it requires all base stations to be tightly synchronized at the physical layer (time and phase) in order to measure TDoA (Time Difference of Arrival). Recent work [27] designs low power backscatter devices that leverage LoRa for localization to achieve high accuracy. However, the system mainly targets indoor applications where software radios can be deployed as base stations to sample the I/Q of the signal and localize the IoT node. Moreover, its current system design [27] supports only a single node. The authors of [34] propose an outdoors localization technique for SigFox IoT devices based on fingerprinting. However, as mentioned earlier, fingerprinting requires constant training and cannot scale to new environments. Finally, there is a lot of work on using UWB or RFID nodes for localization [10, 13, 41]. However, these works focus on indoors and short range as the range of UWB and RFIDs is limited to 10-30 meters [7, 14].

C. IoT Self-Localization: LivingIoT [19] enables self-localization on IoT nodes. It designs a miniaturized device that can be carried by a bumblebee and uses backscatter for communication. The node localizes itself by extracting the angle to the Access Point from the amplitude measurements using an envelop detector. The technique, however, requires the APs to switch the phase across two antennas to change the received amplitude at the IoT node, and hence, cannot be applied to 5G without modifying the base stations. [26] enables self-localization by placing a camera on a WISP RFID but only operates within a range of 3.6 m from the RFID reader.

D. WiFi Based Localization: There has been a lot of work on indoor localization using WiFi [6, 21, 25, 32, 40, 43, 44, 46, 47]. The closest to our work are [21, 40, 43] which estimate the channel impulse response (CIR) and time of flight (ToF) from the WiFi access point (AP). Chronos [40] hops between WiFi channels to compute the CIR at high resolution. However, it requires tight timing coordination with the AP to compensate for carrier frequency offset (CFO) and ensure phase coherence across the measurements. *ISLA*, on the other hand, captures measurements from many frequencies across a wideband without hopping by using the MEMS filter, and hence, does not require any coordination with the base stations. SpotFi [21] combines measurements across antennas with large WiFi bandwidth to separate Line of Sight (LoS) path from multipath reflections in the CIR using MUSIC along two dimensions: ToF and Angle of Arrival (AoA). mD-Track [43] also incorporates Doppler shifts and Angle of Departure (AoD) in addition to ToF and AoA and iteratively refines the CIR to achieve a better estimate of the LoS path. In section 10, we adapt SpotFi's and mD-Track's CIR estimation algorithms to our setting and demonstrate that *ISLA*'s algorithm achieves $4-11\times$ higher accuracy. It is worth noting, however, that for our application, these past works cannot benefit from the doppler or AoA/AoD dimensions.

E. MEMS Filter: Recent work has used MEMS spike-train filters for the application of wideband spectrum sensing [12]. However, [12] can only detect signal power at different frequencies and cannot recover complex I and Q samples needed for estimating the CIR. Furthermore, [12] deals with collisions resulting from aliasing by using co-prime sub-sampling rates. Such approach does not apply in the context of 5G OFDM signals, since, as we show in section 5 the sub-sampling factor can only be a power of 2. *ISLA* instead co-designs the hardware filter together with sampling rate to avoid collisions.

3 Background

A. Spike-Train MEMS Filters: Our work builds on recent advances in MEMS RF filters. MEMS filters can work between a few MHz and 30 GHz and can be integrated with ICs to form a chip-scale RF front-end solution for IoT devices. Past work on MEMS RF filters optimize for filters with a single passband [36, 48], however, the MEMS filter used by

ISLA leverages MEMS resonators that have an assortment of equally spaced resonance frequencies to create a spike train in the frequency domain as shown in Fig. 1(c).

A MEMS filter works by leveraging the inverse piezoelectric effect to convert RF signals into acoustic vibrations for filtering and processing. It then converts acoustic waves in the device back to the RF signals through piezoelectric effect. In this process, the frequency filtering is achieved because not all frequencies can be efficiently converted between RF and acoustic domains. Frequencies that match the resonance frequencies of the piezoelectric structure can go through the conversions with little loss, while other frequencies are filtered out. Hence, the spike train frequencies can be designed by changing the dimension of the piezoelectric material in the MEMS device as well as the placement of electrodes shown under the microscope in Fig. 1(c).

B. Wireless Channel Impulse Response (CIR): The wireless channel can be modeled as the superposition of the signal along all the different paths it takes to travel from the transmitter to the receiver. The channel at frequency f_i can be written as: $h_i = \sum_{l=1}^{L} a_l \exp^{-j2\pi f_i d_l/c}$, where L is the number of propagation paths between the transceivers, d_l is the distance traversed by path l, a_l is the complex path attenuation of path l, and c is the speed of light.

In OFDM systems, data is transmitted over multiple frequency subcarriers $\{f_0, \dots f_{N-1}\}$. If the frequency spacing between these subcarriers is Δf, then the bandwidth spanned by the signal is $B = \Delta f \times (N-1)$. Now, given the channel measurements $\{h_0, \dots h_{N-1}\}$ across these frequencies, the Channel Impulse Response (CIR) can be computed as the inverse FFT of the channel measurements.

$$CIR(\tau) = \sum_{n=0}^{N-1} \left(\sum_{l=1}^{L} a_l \exp^{-j2\pi \frac{d_l}{c} f_n} \right) \exp^{j2\pi\tau f_n} \qquad (1)$$

where $\tau = \{\frac{0}{B}, \dots \frac{(N-1)}{B}\}$ seconds. There are two important things to note here. First, the resolution in Time-of-Flight in the CIR is $1/B$ seconds, that is inversely proportional to the bandwidth B. Hence, larger bandwidth results in higher ToF resolution and more accurate ranging. Second, the maximum unambiguous ToF that can be measured from the CIR is $\frac{(N-1)}{B} = 1/\Delta f$ seconds. This means, if some physical propagation path in the environment has ToF $> 1/\Delta f$ then it would alias and appear at a different tap value in the estimated CIR in Eq. 1. For 5G OFDM signal with $B = 100$ MHz bandwidth and $\Delta f = 60$ kHz , we have a resolution of 10 ns (3 meters) and a range of 16.6 μs (5 km).

4 System Overview

ISLA enables self-localization on narrowband IoT devices by leveraging the MEMS spike-train filter to capture ambient wideband 5G signals. *ISLA*consists of 3 main components:

(1) Capturing the wideband 5G OFDM signal using the MEMS filter: The received 5G signal is passed through the

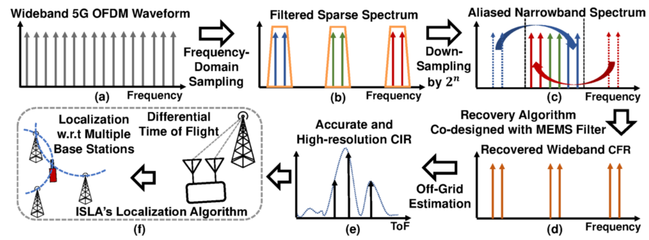

Figure 2: Overview showing the flow of *ISLA*'s system

MEMS filter which samples the OFDM symbol in the frequency domain. Specifically, the MEMS filter passes the OFDM frequency bins that align with the filter passbands while suppressing all other frequency bins. The resulting output from the filter is a sparse spectrum as shown in Fig. 2(b). This sparse signal is then subsampled by the narrowband IoT device significantly below the Nyquist rate (16× lower) which results in aliasing the remaining subcarriers into the narrowband as shown in Fig. 2(c). We co-design the filter hardware with the recovery algorithm to easily reconstruct the wideband OFDM subcarriers as we describe in section 5.

(2) Super-Resolution CIR Estimation: Using the recovered wideband channel measurements, *ISLA* then reconstructs a high resolution Channel Impulse Response (CIR) by leveraging its super-resolution algorithm which estimates the off-grid positions of the propagation paths as described in Section 6. This high-resolution CIR allows *ISLA* to filter out the LoS path from the multipath in the channel for high resolution time-of-flight estimation as shown in Fig. 2(e).

(3) Localization Algorithm: Since the IoT node is not synchronized with the base station, the measured ToF will be corrupted by a timing offset. To address this, *ISLA* leverages two antennas on the IoT device and computes the differential CIR across the antennas to eliminate the synchronization offsets. This results in the locus of the IoT device to lie on a circle that is defined by the locations of the base stations and the angle subtended by the base stations at the IoT device's location, as we explain in Section 7. Thus, by looking at the intersection of such circles, we can accurately infer the position of the IoT device as shown in Fig. 2(f). Finally, we show how to integrate *ISLA* with the 5G-NR standard by addressing additional system challenges in section 8.

5 Capturing 5G Signals Using MEMS Filter

ISLA leverages the MEMS spike-train filters to capture the wideband channel measurements on a narrowband receiver. We explain this sensing process through Fig. 2. Consider a preamble OFDM symbol transmitted from the base station with N subcarrier frequencies at $\{f_0, \dots, f_{N-1}\}$, shown in Fig. 2(a). Let the received time domain symbol be $x(t)$ and its frequency domain representation be $X(f)$. We have $X(f) = \sum_{n=0}^{N-1} c_n h_n \delta(f - f_n)$, where c_n are the data bits modulated onto the subcarriers and h_n are the channel values at f_n. We want to extract this channel information to compute the Channel Impulse Response $CIR(\tau)$. Since the preamble bits c_n are known, we can compensate for c_n and compute the $CIR(\tau)$ by taking an IFFT of the channel values h_n. However, this requires capturing the entire bandwidth of the 5G OFDM signal. Our goal is to recover the CIR using a narrowbandwith. To do so, we leverage the MEMS spike-train filter.

The spike-train filter response is made up of uniformly spaced passbands as shown in Fig. 2(b). The spike-train filter serves to sparsify the OFDM symbol by selectively passing subcarriers that fall inside the MEMS passbands, while suppressing all other frequencies. Let the set of frequencies passed by the spike-train be indexed by M. Then, the frequency domain of the signal $\tilde{X}(f)$ ($\tilde{x}(t)$ in the time domain) after passing through the spike-train filter will be $\tilde{X}(f) = \sum_{i \in M} c_i h_i \delta(f - f_i)$.

This sparse spectrum is shown in Fig. 2(b). Next, the IoT receiver subsamples the signal $\tilde{x}(t)$ using a low-speed ADC that samples at a rate $R = B/P$, where B is the bandwidth of the transmitted symbol and P is an integer corresponding to the subsampling factor. Let $y(t)$ be the subsampled signal, that is, $y(t) = \tilde{x}(P \times t)$, and let $Y(f)$ be its frequency domain representation. Then $Y(f)$ is an aliased version of $\tilde{X}(f)$:

$$Y(f) = \sum_{i=0}^{P-1} \tilde{X}(f + iR) \tag{2}$$

$Y(f)$ will cover a narrow bandwidth equal to R MHz as depicted in Fig. 2(c). The process of aliasing is as follows. Any frequency f_j, $j \in M$, that falls outside the narrowband of the IoT device, will alias onto the frequency bin $\tilde{f}_j$ inside the narrowband after subsampling, such that $f_j - \tilde{f}_j = z \times R$, where z is some integer. Note that for every f_j, we have a unique $\tilde{f}_j$. So given the measurement at the aliased frequency $\tilde{f}_j$, we can potentially recover the channel value h_j at the corresponding unaliased frequency f_j.

However, recovering these channel values from the aliased spectrum is non-trivial because multiple of the frequency subcarriers passed by the spike-train filter may collide by aliasing on top of each other and summing up. This is unfavorable since now we are unable to extract the channel values for any of the colliding frequencies. Past work addresses this by leveraging multiple co-prime subsampling factors, which ensures that the same frequencies don't collide repeatedly.

Unfortunately, we do not have such flexibility to choose any sub-sampling factor here. This is because in order to recover the channel value h_j from the aliased frequency $\tilde{f}_j$, we need to ensure that the complex scaling factor $c_j \times h_j$ encoded on subcarrier f_j remains preserved upon aliasing. This is crucial because the wireless channel information is contained inside this scaling factor. The following lemma states the condition that ensures this:

Lemma 5.1. *For a sub-sampling factor P and N OFDM subcarriers, the complex valued scaling factors for each subcarrier will be preserved upon aliasing if $N = z \times P$, for some integer z, given the aliasing results in no collisions.*

The proof for the above lemma is in Appendix A. Thus, to be able to recover channel values, we are restricted to subsample the signal by an integer factor of N. Further, since the OFDM subcarriers in the 5G standard are set to powers of 2, we can only subsample the wideband signal by powers of 2.

Due to this lack of choice in subsampling factors, we instead shift our focus on designing the spike-train filter such that the frequencies passed by the filter do not collide upon aliasing. We achieve this by leveraging the structured periodic sparsity of the spike-train, and design a filter that ensures no collisions for the given subsampling factor P.

Doing so significantly simplifies our recovery algorithm. In particular, given that (1) the frequency response of the spike-train filter and its collision-free aliasing patterns are known, and that (2) the scaling factors at the frequency subcarriers remain preserved upon aliasing, we can now simply rearrange the frequencies in Y(f) to their corresponding unaliased frequency positions as shown in Fig. 2(d). Further, we can extract the channel values at these unaliased frequencies by dividing the complex scaling factor $c_j \times h_j$ by the known preamble bit c_j. Thus, by leveraging the spike-train filter, *ISLA* is able to extract wideband channel values on a narrow band IoT device. Next, we discuss the design parameters of the spike-train filter that ensures no collisions.

Spike-Train Filter Design: We explain the spike-train filter design with a specific example, shown in Fig. 3(a). Let the wideband transmitted OFDM signal (B MHz bandwidth) be comprised of 32 frequency subcarriers, indexed from -16 to 15, with 0 denoting the carrier frequency bin. From Lemma 5.1, we want the subsampling factor P to divide $N = 32$. So we choose $P = 4$, that is, the IoT receiver subsamples the signal by $4\times$. This implies that the IoT receiver is only able to capture $\frac{N}{P} = 8$ frequency bins centered around the carrier frequency as shown by the shaded region in Fig. 3(a). Let this narrow band set of frequencies be denoted as f_{NB}.

Recall that when you subsample a B MHz signal by $P\times$, then all frequency subcarriers spaced by $R = \frac{B}{P}$ MHz will alias onto the same frequency bin in the narrow band spectrum. Here, this translates into all frequencies spaced by 8 subcarriers aliasing onto the same narrowband bin. This is depicted in Fig. 3(a) through the color coding scheme. For instance, the subcarriers at $\{-9, -1, 7, 15\}$ (represented as purple colored) would all appear at frequency bin -1 in the narrow band spectrum upon aliasing. For a given subcarrier k in the narrow band spectrum, that is, $k \in \{-4, \ldots, 3\}$, let us denote the set of subcarriers that would alias into k as I_k. So we have $I_{-1} = \{-9, -1, 7, 15\}$.

The spike-train filter will selectively pass frequency subcarriers in the wideband OFDM signal, which after aliasing can be recovered from the narrow band signal at the receiver. Let the set of frequency subcarriers passed by the spike-train filter be denoted by f_M, where $M \in [-15, \ldots, 16]$. We want the following conditions to hold:

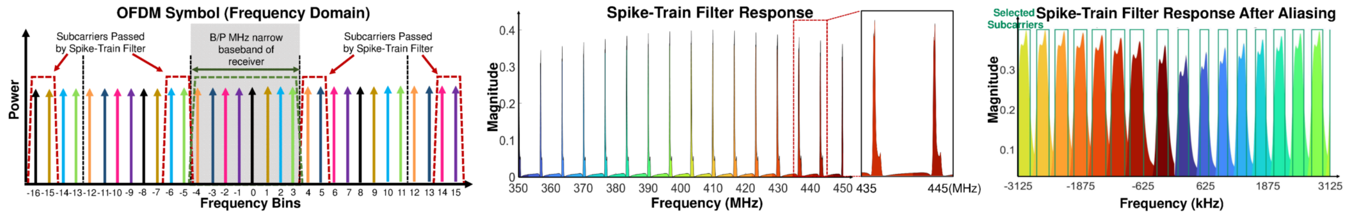

(a) Spike-Train Filter Parameters (b) Spike-Train Filter Frequency Response (c) Aliased Frequency Response

Figure 3: (a) MEMS Filter Parameters that ensure zero collisions while recovering maximum channel information. (b) Frequency response of MEMS spike-train filter. (c) Aliasing pattern of spike-train filter frequency response.

1. *No Collisions:* To ensure that we can successfully recover the wideband channels, no two subcarriers in f_M should alias and collide in the same narrowband frequency bin upon subsampling. To achieve this, the spike-train filter must satisfy: *For any set I_k where $k \in \{-4, \dots, 3\}$, f_M must contain at most one subcarrier from I_k.*
2. *Extract Maximum Possible Channel Values:* Given that the narrowband spectrum spans 8 frequency subcarriers, this means that the receiver can successfully recover at most 8 channel values after subsampling. In the presence of noise, we want to recover as many channel measurements as possible for robustness. Hence, every narrowband subcarrier in f_{NB} should yield one channel measurement from the wideband signal. This translates to: *For any set I_k where $k \in \{-4, \dots, 3\}$, f_M must contain at least one frequency subcarrier from I_k.*
   1 and 2 put together, dictates that the spike-train filter should pass *exactly one* frequency subcarrier from each I_k.
3. *Span the Wideband OFDM symbol:* To retain the high ToF resolution, we want the set of frequencies in f_M to span the entire wideband signal.

The above conditions can be met leveraging the structured sparsity in the spike-train filter response. Specifically, we can design three key parameters of the spike-train filter: (1) spacing between consecutive spikes ΔF, (2) width of the spikes ΔS, and (3) the starting frequency subcarrier f_M^0 in the spike-train, to follow Lemma 5.2. We prove in Appendix A that such a filter response satisfies the above conditions.

Lemma 5.2. *Consider an OFDM symbol with N frequency subcarriers, indexed as $\{f_{\frac{-N}{2}}, \dots, 0, \dots, f_{\frac{N}{2}-1}\}$ with inter-frequency spacing of Δf, and a narrowband receiver that subsamples by $P\times$. If P^2 divides N, then the ideal filter parameters that meet all three requirements are: (1) $f_M^0 = f_{\frac{-N}{2}}$, (2) $\left(\frac{N}{P^2} - 1\right) \times \Delta f < \Delta S < \frac{N}{P^2} \times \Delta f$, and (3) $\Delta F = \frac{N}{P}\left(1 + \frac{1}{P}\right) \times \Delta f$.*

Furthermore, we can achieve the required filter response by designing the topology of the MEMS resonators, which we explain in more details in Appendix B.

In Fig. 3(a), we show the ideal frequency response of the spike-train filter designed with the above parameters as the red dotted line. In theory, such a filter should allow us to leverage all f_{NB} subcarriers to recover the wideband channel measurements from the aliased signal. However, in practice, MEMS spike-train filters are non-ideal i.e., the roll-off of the passband boundaries are not as sharp as perfect rectangular functions, the spikes are not perfectly equally spaced, and the passband widths are not identical. These imperfections can be observed in the frequency response shown in Fig. 3(b). As a result of these non-idealities, there will still be collisions at the boundary regions of the spikes after aliasing, as shown in Fig. 3(c). To avoid collisions from polluting our CIR estimates, we only consider the subcarriers that do not collide as shown in Fig. 3(c). However, this results in non-uniform sampling of the OFDM subcarriers across the wideband channel. In sec. 6, we show how to leverage *ISLA*'s super-resolution algorithm to recover high resolution CIR estimates from these non-uniform channel measurements.

Tradeoff Between Range and Resolution: Recall from section 3 that the resolution in ToF depends on bandwidth, whereas the maximum unambiguous ToF (range) depends on the inter-frequency spacing between channel measurements. In the 5G OFDM signal with bandwidth $B = 100$ MHz and subcarrier spacing $\Delta f = 60kHz$, *ISLA* is able to retain the high ToF resolution of 10 ns (3 m) by collecting wideband channel measurements that span the entire 100 MHz. However, in doing so, the frequency spacing between the channel measurements in *ISLA* increases, thus reducing the maximum ToF range. Specifically, the frequency spacing increases by $P = 16\times$ in *ISLA*, thus reducing the maximum range from 5 km to 312 meters. This is an issue since now it becomes difficult to identify the LoS path from the CIR for localization. You could have the case where the LoS path is at 200 meters but a reflected path at 400 meters aliases and appears at the bin corresponding to 88 meters in the CIR. Thus, you cannot simply pick the first peak as LoS.

To address this, *ISLA* combines the wideband channel measurements from the spike-train filter, h_M, with the narrowband channel measurements h_{NB} collected at the subcarriers f_{NB}, and formulates a joint optimization with both these channels to estimate the CIR. Since the narrowband channel measurements h_{NB} retain the same subcarrier spacing of $\Delta f = 60kHz$, it increases the effective maximum ToF range back to 5 km, thus resolving the LoS ambiguity in the CIR.

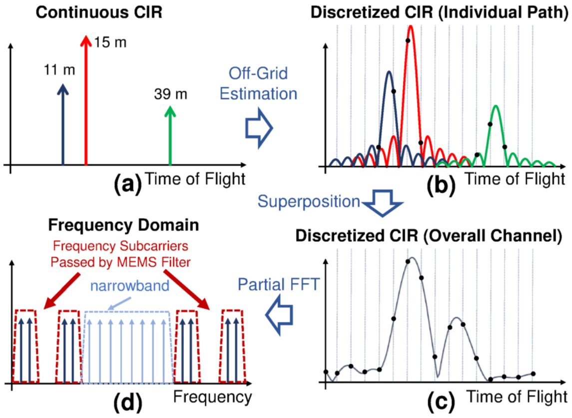

Figure 4: Signal paths to measured channel forward function

6 Super-Resolution CIR Estimation

Here we describe our super-resolution algorithm that can retrieve high resolution ToF estimates τ_l's along with the associated complex attenuations a_l for the L multipath components in the channel. As discussed in Sec. 5, the IoT device can recover channel measurements $h_{tot} = h_M \cup h_{NB}$ at the subcarriers $f_{tot} = f_M \cup f_{NB}$ where f_M are recovered from the spike-train filter and f_{NB} without the filter. Since these channel values are sampled at non-uniformly spaced frequencies, we cannot apply standard super-resolution algorithms like MUSIC with spatial smoothing [21, 44] as they require uniform measurements. Instead, we optimize for the channel impulse response in the continuous time domain by leveraging an off-grid estimation technique that can estimate high resolution ToF values from the channel information.

We begin by framing this as an inverse problem. We start by modeling the forward operator $\mathcal{F}$: $h_{tot} = \mathcal{F}(\tau_1, \ldots, \tau_L, a_1, \ldots, a_L)$, which maps physical path parameters to the wireless channel. $\mathcal{F}$ comprises of the following distinct transformations, as illustrated in Fig. 4:

(1) CIR in Continuous Domain: (Fig. 4(a)) Given path parameters $\{\tau_1, \ldots, \tau_L, a_1, \ldots, a_L\}$, the continuous domain CIR can be written as: $CIR_{cont} = \sum_{l=1}^{L} a_l \delta(\tau - \tau_l)$, with each path represented as an impulse positioned at its respective ToF τ_l, and scaled by its complex attenuation a_l.

(2) Off-Grid Estimation: (Fig. 4(b)) The OFDM symbol spans a bandwidth B MHz and comprises of N subcarriers. Due to this discretization and truncation in the frequency domain, the observed CIR at the receiver will also be discretized, and computed on the grid defined by τ_g, where $\tau_g = \{\frac{0}{B}, \ldots, \frac{(N-1)}{B}\}$. However, as with most natural signals, the ToFs of the physical propagation paths τ_l will rarely align with this discretized τ_g grid, that is, the τ_l's will lie at an off-grid position. As a result, the leakage from the continuous off-grid CIR component from path l to the discrete CIR grid positions at τ_g can be computed as $CIR^l(\tau_g) = a_l \psi_N(\tau_g - \tau_l)$, where ψ_N is the discretized sinc function defined as:

$$\psi_N(\tau) = \frac{\sin(\pi\tau)}{\sin\left(\frac{\pi\tau}{N}\right)} \exp\left(-\pi j \left(\frac{N-1}{N}\right)\tau\right) \tag{3}$$

(3) Superposition: (Fig. 4(c)) With multiple propagation paths in the channel, the net observed CIR at the receiver is the sum of the CIR profiles contributed by each propagation path: $CIR^{net}(\tau_g) = \sum_{l=1}^{L} a_l \psi_N(\tau_g - \tau_l)$.

(4) Discrete Fourier Transform: (Fig. 4(d)) Finally, the channel h_{tot} can be computed by sampling the corresponding frequencies f_{tot} from the DFT of the superposed CIR. Let us denote the $N \times N$ Fourier matrix as $\mathbf{F}_N$, and let $\mathbf{V}$ be the matrix that chooses the rows corresponding to f_{tot} from $\mathbf{F}_N$. Then we have: $h_{tot} = \mathbf{V}\,\mathbf{F}_N\; CIR^{net}$ where CIR^{net} is a $N \times 1$ dimension vector.

Putting the above four transformations together, the forward operator $\mathcal{F}$ can be expressed as:

$$h_{tot} = \mathcal{F}(\{\tau_l, a_l\}_{l=1}^{L}) = \mathbf{V}\,\mathbf{F}_N \Psi \vec{a} \tag{4}$$

where Ψ is a $N \times L$ matrix with $\Psi_{i,j} = \psi_N(\tau_i - \tau_j)$, and $\vec{a}$ is a $L \times 1$ vector comprising the complex attenuations a_l for each path. Now that we have the forward operator, the inverse problem to retrieve the path parameters from observed channel vector h'_{tot} can be formulated as a L-2 minimization:

$$\{\tau_l^*, a_l^*\}_{l=1}^{L} = \underset{\tau_1,\ldots,\tau_L,a_1,\ldots,a_L}{\arg\min} \|h'_{tot} - \mathbf{V}\mathbf{F}_N\Psi\vec{a}\|^2 \tag{5}$$

Solving the Optimization: Note that if we are given Ψ, then Eq. 5 becomes a linear optimization problem in $\vec{a}$. Thus, given Ψ, the closed form solution for $\vec{a}$ that minimizes Eq. 5 is $\vec{a} = (\mathbf{V}\mathbf{F}_N\Psi)^{\dagger} h'_{tot}$, where $\dagger$ represents the pseudo-inverse. Thus the objective function in Eq. 5 can be rewritten as:

$$\begin{aligned} \{\tau_l^*\}_{l=1}^{L} &= \underset{\tau_1,\ldots,\tau_L}{\arg\min} \|h'_{tot} - \mathbf{V}\mathbf{F}_N\Psi(\mathbf{V}\mathbf{F}_N\Psi)^{\dagger} h'_{tot}\|^2 \\ \text{s.t.} \quad & \tau_l \geq 0 \quad \forall\, l \in \{1, 2, \ldots, L\} \end{aligned} \tag{6}$$

The objective function is now reduced to just the ToF variables τ_l's. This optimization problem is non-convex and constrained, and we use the well-known interior-point method to solve this [8]. For the initialization point to the optimization algorithm, we use approximate ToF values from the CIR computed by taking the inverse FFT of the observed channel h'_{tot}. While these ToF estimates are distorted by the discretization and superpositioning artifacts described previously, it gives a good starting point for the optimization.

Also, note that the number of paths N in the wireless channel is not known a priori. As we keep increasing the number of paths N that the algorithm is initialized with, it keeps finding a better and better fit to the channel data, and after a point, starts overfitting to the noise. In order to avoid overfitting and yet yield accurate estimates for the path parameters, we run the optimization problem multiple times, each time increasing the number of paths it is initialized with by 1. We terminate the algorithm when the decrease in the value of the objective function falls below some threshold ε, and set the current value of N to be the number of paths in the channel.

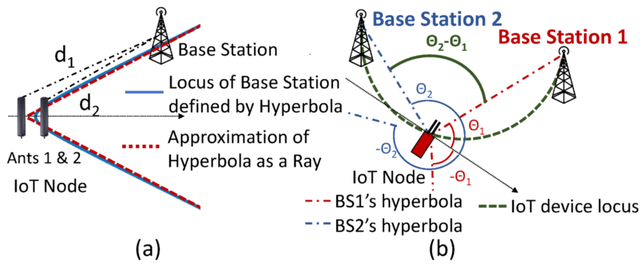

Figure 5: *ISLA*'s Localization Algorithm

7 *ISLA*'s Localization Algorithm

The above off-grid estimation algorithm gives us highly precise ToF estimates for the propagation paths. However, since the 5G base stations are not time synchronized with the IoT device, there is going to be an offset between the sampling clocks in their RF chains. As a result, the measured ToF at the IoT node also includes delays from the sampling time offset (STO) between the different base stations and the IoT node, and hence cannot provide accurate distance estimates.

To address this, *ISLA* leverages two antennas on the IoT node to compute the differential ToF rather than the absolute. The key idea here is that while the absolute ToF measurements are corrupted by synchronization offsets, these offsets are constant across the two antennas on the IoT node. Hence, the offsets can be eliminated by differencing the two measurements. Let the ToF values to the two antennas be τ_1 and τ_2, and their corresponding distances be d_1 and d_2, as denoted in Fig. 5(a). Then the locus of the base station from the IoT device's frame of reference is a hyperbola with the two antennas being the foci, and the difference in distances to the two foci equaling $d_2 - d_1$. At large distances, this hyperbola can be approximated as two rays along the asymptotes of the hyperbola, depicted by the red dashed lines in Fig. 5(a).

By overhearing packets from different base stations, the IoT device can infer the locus of each base station to lie on approximated rays originating from the IoT device's location. This is shown in Fig. 5(b), where base station 1 can lie on the rays at angles θ_1 or $-\theta_1$, and similarly the base station 2 can lie on the rays at angles θ_2 or $-\theta_2$. Both θ and $-\theta$ are possible since there is the ambiguity that the signal might have arrived from the front or the back of the device. Given this, we can see that the angle subtended by the two base stations at the location of the IoT device will be $\|\theta_2 - \theta_1\|$, and this is going to be constant irrespective of the orientation of the IoT node. (There is ambiguity in that the angle subtended can also be $\|\theta_2 + \theta_1\|$, and we will address this shortly).

Given the angle subtended by the base stations and the known locations of the base stations, according to the Inscribed Angle Theorem, we can determine the locus of the IoT device to lie on the arc of a circle, where the line segment connecting the two base stations is the chord and the corresponding inscribed angle is equal to the angle subtended by the base stations. This is illustrated in Fig. 5(b) as the green dashed arc. Leveraging different pairs of base stations, *ISLA* can draw multiple such arcs and the intersection points of these arcs will give us the IoT device's location.

Sources of Ambiguity: There are some sources of ambiguity that need to be resolved. First, the angle subtended by the two base stations in Fig. 5(b) could also be $\|\theta_2 + \theta_1\|$, and second, the arc drawn with the base stations at the end points could also be pointing towards the north rather than south, as depicted in Fig. 5(b). These ambiguities can be resolved easily by leveraging 4 base stations as anchor points. Keeping one base station common, we have three base station pairs which yields three unique arcs. Only the right configurations of angles subtended and arcs drawn will give us a common intersection point for all three arcs. *ISLA*'s localization algorithm tries all configurations and picks the one where all arcs coincide at the same point.

8 Integrating *ISLA* with 5G-NR Standard

Similar to the LTE standard, the 5G-NR packet consists of 10 subframes, each of duration 1 ms [28]. To allow for coherent packet demodulation, the 5G frame appends known preamble bits on each subframe which enables channel estimation and correction across the entire bandwidth of the 5G channel. Additionally, in the first subframe of the packet, the base station also includes all information required by devices to associate with the network, which comprises of the synchronization signals (PSS and SSS frames) for CFO correction and frame timing, and the Base Station ID. To allow every device in the network to receive this critical information, it is always encoded in the narrowest supported bandwidth of the wideband packet, which is 4.32 MHz in the 5G standard [28].

ISLA's hardware circuit, discussed in Section 9, is designed such that it can switch between capturing the 6.25 MHz narrowband spectrum, or the wideband spectrum via the spike-train filter. *ISLA* begins by capturing the first subframe of the 5G packet through its narrowband RF path, and extracts the synchronization frames and base station ID encoded in the narrowband subcarriers of the wideband packet. Using publicly available databases like [1], *ISLA* can retrieve the location of the Base Station given its ID. The synchronization frames help eliminate coarse CFO and SFO. From the subsequent subframes, *ISLA* first estimates the narrowband channel, and then switches to the RF path with the spike-train filter to sense wideband channel. Note that *ISLA* does not need to meet tight timing constraints to switch since each subframe lasts 1 ms and there are multiple such subframes in each packet that can be leveraged for channel estimation. Thus, *ISLA* can simply skip a subframe while switching.

However, because *ISLA* captures the narrowband channel and wideband channel from different subframes, there is going to be an additional phase accumulation between the two measurements due to residual CFO. To address this, we slightly modify Eq.6, and the detailed description for this modification is presented in Appendix C.

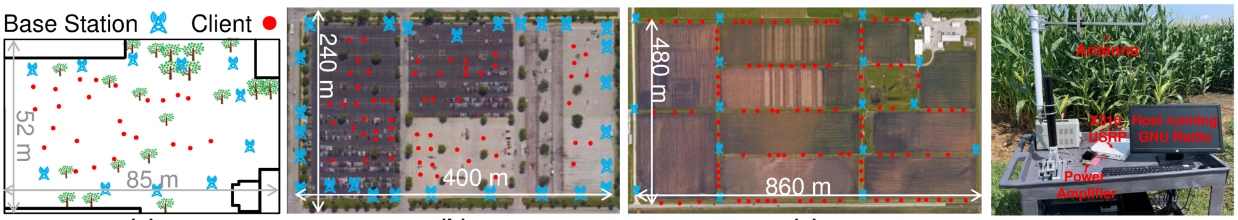

(a) (b) (c) (d)

Figure 6: Ourdoor Experiment Testbeds: (a) Campus testbed surrounded by buildings. (b) Parking lot testbed. (c) Agricultural farm testbed. (d) Prototype base station in the agricultural farm testbed.

9 System Implementation

System Design: We have built a prototype *ISLA* device by combining our MEMS spike-train filter with commodity, off-the-shelf, low-power components. Figure 7(a) shows the circuit diagram, and Fig. 7(b) shows the actually prototype. It receives ambient 5G transmissions with two antennas followed by identical RF chains. Depending on whether the IoT devices wants to receive the full 100 MHz spectrum using the spike-train filter or the narrowband spectrum, the RF chains can switch between two paths: (1) the received wideband spectrum first be filtered by the MEMS spike-train filter, and then down-converted and sampled without using the anti-aliasing filter. (2) the MEMS spike-train filter is bypassed but the down-converted signal will first go through an anti-aliasing filter before sampling. We select between the two paths using RF switches controlled by a single microcontroller.

Implementation: We fabricated a MEMS spike-train filter at 400 MHz center frequency. However, due to the strong interference from the amateur radios in this band, we were not able to run experiments outdoor using this filter. Hence, the above prototype was only used indoors. In the outdoor experiments, we transmitted in a vacant 100 MHz wide spectrum between 950 and 1050 MHz, and we emulate the IoT radio front-end described above with the MEMS spike-train filters in digital using an X310 USRP software-defined radio (SDR). We would like to note that in practical deployments we do not expect interference to play a major issue since *ISLA* will be deployed in the proprietary frequency bands licensed by cellular companies, which in turn will have limited interference.

The X310 SDR has two identical RF chains, and can sample the full 100 MHz bandwidth with UBX160 daughterboards. To emulate the MEMS spike-train in digital, we first measure the spike-train filter frequency response once using a vector network analyzer (VNA), and we apply this filter frequency response to the received signals sampled at 100 MHz. Then, we downsample the filtered signal by simply keeping every 16th sample. This is equivalent to filtering the RF signal in analog and sample it below the Nyquist sampling rate. We also used a bandpass filters between the antenna and SDRs to remove out-of-band interferences and synchronized the two RF chains in time and phase through the GNU Radio Python API. In section 10.3, we present mircobenchmarks demonstrating the equivalence between applying the filter in digital and the above hardware prototype.

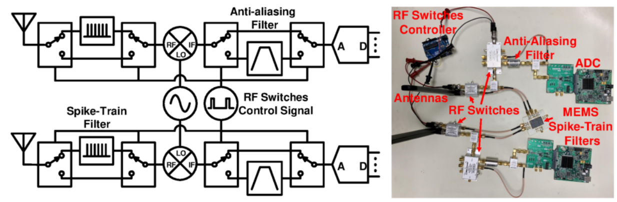

(a) Circuit Diagram (b) Prototype Circuit

Figure 7: *ISLA* Prototype Circuit

Testbed: Additionally, we also built 5G base station TX prototypes to transmit ambient 5G communication signals. As shown in Fig 6(d), the base station prototype consists an X310 USRP SDR with a UBX160 daughterboard, a 9 dBi Yagi directional antenna, and an RF Bay MPA-22-30 30 dB power amplifier. The base stations transmit 100 MHz OFDM packets. Using five base station prototypes, we created three testbeds with different dimensions and at different locations to conduct our experiments. Figure 6 shows the satellite images of our testbeds with the base stations and clients locations marked. The first testbed is 85 m long and 52 m wide on a university campus, surrounded by buildings on all sides. We designated 11 basestation locations in this testbed and chose five of them for each experiment. The second testbed is a 400 m by 240 m parking lot with 27 base station locations. The third testbed is at a 102 acre farmland with 860 m length 480 m width. We selected five out of the 17 potential locations to place the base stations in each experiment. For ground truth locations, we used differential GPS RTK with real-time RTCM correction data, which provides centimeter-level positioning accuracy.

10 Experimental Evaluation

10.1 Baselines

(1) *Spot-Fi:* [21] proposes a 2D MUSIC algorithm with spatial smoothing, which can localize clients by separating the multipath components jointly along the ToF and AoA domains.
(2) *mD-Track:* [43] separates propagation paths by leveraging multiple dimensions of the wireless signal (ToF, AoA, AoD and Doppler), and proposes an iterative algorithm that goes through multiple rounds of error computation and path re-estimation. In our experimental setup, leveraging the AoD and Doppler dimensions provides little benefit since the base

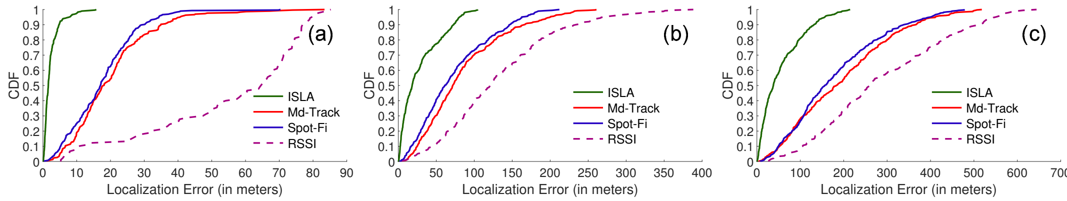

Figure 8: *ISLA*'s localization accuracy compared against baselines across different testbeds: (a) Campus (b) Parking lot (c) Farm.

station is equipped with a single antenna and the IoT device does not have high mobility relative to the base station.

Note that, systems like Spot-Fi and mD-Track were not designed for ambient localization, and thus need to be adapted here. Specifically, we leverage the ToF estimates provided by these baselines for the LoS path, and in turn self-localize the client by computing the relative ToF, as described in Section 7.

(3) *RSSI:* Past work leverages RSSI measurements to localize clients in outdoor cellular networks, by either using approximate path loss models for trilateration, or by using the known locations of nearby cells as coarse estimates. We implemented one recent RSSI baseline [9].

(4) *Spike-train filter-adapted baselines:* To provide a fair comparison against *ISLA*, we modify Spot-Fi and mD-Track to leverage the spike-train filter and utilize the wideband channel measurements for localization. It is non-trivial to adapt Spot-Fi for the spike-train filter since the spatial smoothing technique used in Spot-Fi requires uniformly spaced channel measurements across frequency, whereas the spike-train filter samples the OFDM frequency bins non-uniformly. To address this, we restructure the spatial smoothing subarray from [21] that allows Spot-Fi to be applied across the non-uniform frequencies sampled by the spike-train filter.

10.2 Results

Unless otherwise specified, for all results, we utilize 5 randomly chosen base stations as the anchor points.

A. Localization Accuracy Comparison against Baselines: We compare *ISLA*'s localization against the baselines in Fig. 8. Note that, while *ISLA* is designed specifically to leverage the wideband channel sensed by the MEMS filter, the baselines are implemented without modification and thus utilize only the narrowband channel for localization.

From Fig. 8, *ISLA* achieves a median localization accuracy of 1.58 meters in the campus testbed, 17.6 meters in the parking lot testbed, and 37.8 meters in the farm testbed. Across the same three testbeds, Spot-Fi achieves median accuracies of 17.05 meters, 61.2 meters and 156.6 meters, whereas mD-Track achieves 18.11 meters, 71.8 meters, and 183.1 meters respectively. Thus, *ISLA* improves the localization accuracy over Spot-Fi and mD-track by $\sim 11\times$ in the campus testbed, and by $\sim 4\times$ in the parking lot and farm. *ISLA* is able to achieve such high gains since it leverages the spike-train filter to sense wideband channel on the narrowband device, which allows for much higher resolution compared to the baselines operating solely in the narrowband. Further, the localization improvement over the narrowband baselines is most significant in the campus testbed, since it has the most multipath from surrounding buildings, and thus ToF resolution is critical to separate out the LoS path from reflections.

Lastly, the RSSI baseline achieves median accuracies of 64.54 meters, 120.7 meters, and 260.8 meters respectively across the three testbeds. RSSI based methods generally have poor performance, as they tend to oversimplify path loss models that map RSSI values to distance, which does not hold for real world multipath channels.

B. Comparison against Spike-train-adapted Baselines: Next, we evaluate how leveraging the spike-train filter would benefit the performance of our narrowband baselines. Fig. 9 shows the CDF of localization accuracy comparing *ISLA* against the modified baselines that utilize the wideband channel from the spike-train filter. The RSSI baseline is not included here since its localization performance does not depend on bandwidth. Compared to its narrowband implementation, Spot-Fi's median accuracy improves to 11.08 meters in the Campus testbed, 49.07 meters in the Parking Lot, and 137.76 meters in the farm. Similarly, mD-Track's median performance improves to 15.48 meters, 51.45 meters and 103.78 meters in the three testbeds respectively. Thus, Spot-Fi and mD-Track see improvements in localization accuracy by up to 54% and 76% respectively. This shows that other localization techniques can also benefit from the wide-band channel sensing capabilities enabled by the spike-train filter.

Additionally, Fig. 9 shows that given the same channel information, *ISLA*'s off-grid CIR estimation algorithm is able to better resolve and estimate the relative ToF compared to Spot-Fi and mD-Track. This is because these baselines were designed to leverage multiple information dimensions to separate out the multipath components, with both baselines leveraging 3 or more antennas for separation in the AoA domain, and mD-Track further using the additional dimensions of Doppler and AoD as well. In contrast, here the IoT device has to separate out multipath in the ToF domain alone, and *ISLA* is able to achieve very accurate localization owing to its off-grid estimation algorithm.

C. *ISLA* **Leveraging Different Amounts of Spectrum:** In this experiment, we compare *ISLA*'s localization algorithm applied across three different amounts of spectrum utilization — (1) *ISLA* applied only to the wideband sparse channel sensed by the spike-train filter (without combining with narrowband channel), (2) *ISLA* applied only to the narrowband channel of

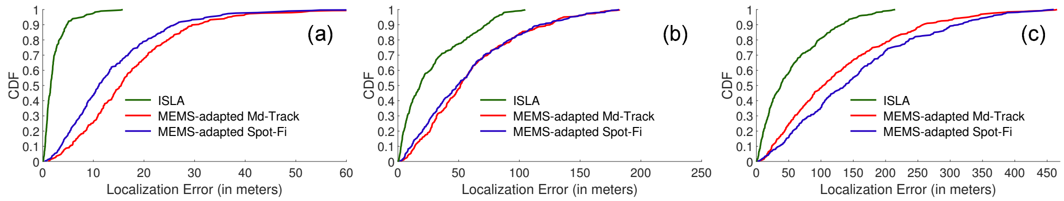

Figure 9: *ISLA*'s localization accuracy compared against MEMS filter adapted baselines at: (a) Campus (b) Parking lot (c) Farm.

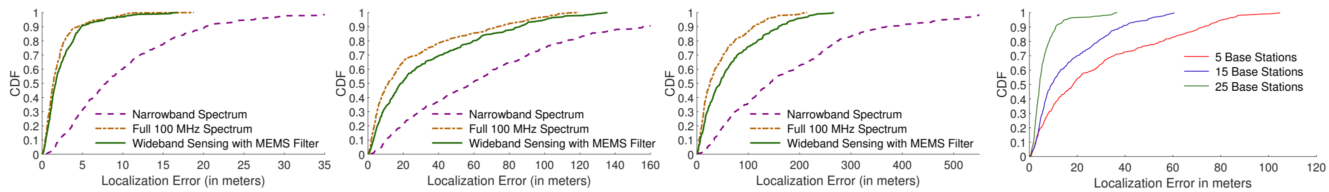

(a) Campus (b) Parking Lot (c) Agricultural Farm (d) *ISLA*'s localization error vs #BSs

Figure 10: (a-c) Comparison of *ISLA*'s localization accuracy when leveraging different amounts of spectrum across all three testbeds. (d) *ISLA*'s localization error with different number of visible base stations.

IoT device, and (3) *ISLA* applied across the entire 100 MHz bandwidth of the received 5G signal. Fig. 10 plots the CDF of localization accuracy achieved across the three testbeds.

ISLA applied on the narrowband channel performs the poorest, achieving median accuracies of 7.9 meters, 58.9 meters and 142.52 meters in the campus, parking lot and farm testbeds. In contrast, *ISLA* along with the spike-train filter can achieve corresponding median accuracies of 1.68 meters, 18.8 meters and 45.04 meters. Thus, *ISLA* along with spike-train achieves an improvement in localization accuracy of $3.16\times - 4.7\times$ compared to *ISLA* applied in the narrowband spectrum, despite both baselines capturing the same amount of channel measurements. The advantage of spike-train stems from the fact that it enables the narrowband receiver to capture channel measurements that span a much larger bandwidth, which results in much higher ToF resolution.

On the other hand, *ISLA*'s localization algorithm applied on the full 100 MHz spectrum achieves median accuracies of 1.38 meters, 11.44 meters and 25.8 meters respectively on the three testbeds. Thus, *ISLA* with the spike-train filter reduces the localization accuracy by only $1.21\times$, $1.64\times$, and $1.74\times$ respectively compared to this upper bound. This demonstrates that the spike-train filter can enable a narrowband device to achieve localization accuracy within a factor of $2\times$ compared to a broadband receiver, despite the fact that it subsamples the signal by $16\times$ below Nyquist.

D. Localization with Number of Anchor Base Stations: In Fig. 10(d), we compare *ISLA*'s localization performance with 5, 15 and 25 base stations used as anchor points respectively, in the parking lot testbed. With 5 base stations, *ISLA* achieves a median accuracy of 17.6 meters, which improves to 9.27 meters with 15 base stations, and 4.26 meters with 25 base stations. This improvement becomes even more significant at the tail, with *ISLA* achieving 90^{th} percentile accuracy of 73.16 meters with 5 base stations, which improves to 10.9 meters accuracy with 25 base stations at 90^{th} percentile. Thus, leveraging more base stations can significantly improve the localization accuracy achieved by *ISLA*.

E. Tracking Objects: We move the IoT device across an L-shaped trajectory (160 meters in length and 85 meters in width) in the parking lot testbed, and collect packet transmissions from the base stations at different points along this trajectory. In this experiment, we pick 7 fixed base stations to utilize as anchor points, and we show the ground truth trajectory and corresponding estimated trajectory by *ISLA* in Fig. 11(a). As can be observed, *ISLA*'s high localization accuracy allows to faithfully capture the shape of the ground truth trajectory.

10.3 Microbenchmarks

A. CIR Estimation using Fabricated MEMS Spike-train Filter: To verify the equivalence between our outdoor implementation and using the prototype with the fabricated MEMS spike-train filter at 400 MHz, we conduct indoor experiments at 400 MHz. Specifically, we evaluate the error in reconstructed CIR and estimated ToF values between the prototype with the fabricated filter and *ISLA* with the digital filter implementation. In Fig. 11(b), we show the CDF of the errors in ToF values (converted to distance (meters)) recovered by the two approaches, for both LoS and NLoS paths. We can see that the position of the LoS path in the CIR estimated from both approaches are very close, with the median error between their estimates being 0.075 meters. The error in the NLoS paths is higher, with a median error of 1.05 meters. However, this will not affect the localization performance between the two since localization only uses the LoS path. This microbenchmark demonstrates that *ISLA*'s approach of applying the filter and subsampling in digital is equivalent to using the fabricated filter from a localization perspective, and that the results shown in this paper are representative of a fully implemented system.

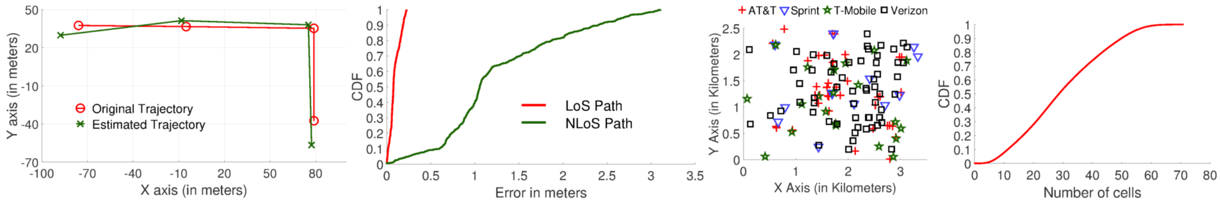

(a) Tracking Object Trajectory (b) Fab. MEMS filter vs *ISLA*'s Imp. (c) 4G BS Density (d) # of Visible BSs

Figure 11: (a) Using *ISLA* to track object trajectory. (b) ToF difference between *ISLA*'s prototype with fabricated MEMS filter and digitally implemented MEMS filter. (c) Deployment of 4G base stations in the downtown area of a major US city. (d) Number of visible 4G base stations at various downtown locations.

Direction	NW	NE	SE	SW
Median	1.3535 m	1.3544 m	1.3267 m	1.3681 m
Std Dev	0.4948 m	0.6026 m	0.4908 m	0.512 m

Table 1: Invariance of Localization Error to Orientation

B. Density of Deployed Base Stations: In Section 10.2D, we have shown that *ISLA*'s localization accuracy increases substantially as we use more anchor base stations. Here, we study the distribution of how many base stations can the client overhear at a given location. Using publicly available databases [1], we retrieved the locations of 4G LTE base stations belonging to 4 major carriers in the United States. We chose 4G LTE for this analysis since 5G deployment is still in its nascent stage in the USA, but we expect the target coverage for 5G networks to exceed the 4G deployment.

In Fig. 11(c), we show the scatter plot of the 4G base stations located in the downtown area of a major metropolitan city in the USA. Using the cell coverage information provided in [1] for the different base stations, in Fig. 11(d), we plot the CDF of the number of base stations that the client can overhear at different locations on the map. We can see that at the 10^{th} percentile, the number of visible base stations is 11, thus implying that less than 10% of client locations see less than 11 base stations. Further, the median number of base stations visible to the client is 29. This demonstrates that the cellular deployment is dense enough to allow many anchor points, which in turn can achieves high localization accuracy.

C. Invariance to Orientation: Here, we demonstrate that the localization performance is independent of the orientation of the IoT device. This is because the arcs that define the locus of the IoT node, depend only on the angle subtended by the base stations at the IoT device's location, which is invariant to device rotation. At a given location in our campus testbed, we orient the IoT device along 4 different directions and perform 100 localization experiments at each orientation. From Table 1, we can see that the median and standard deviation in localization error is almost the same across the 4 orientations, thus demonstrating invariance to orientation.

11 Limitations and Discussion

- *Power Footprint:* To enable ambient localization, *ISLA* leverages a second antenna and RF chain, which increases the power footprint of the IoT device. However, we would like to note that the power overhead of an additional RF chain is going to be lower than that of a GPS module, which is the likely alternative for localization. This is because the additional RF chain on the IoT device is going to operate in the narrowband with very low sampling rates, whereas GPS incurs high operational power since it needs to receive and correlate long sequences to get the signal power above the noise floor for GPS lock acquisition. Hence, while *ISLA*'s design does lead to an increased power footprint, it is still a better alternative compared to GPS.
- *Loss of SNR:* Since the MEMS spike-train filter is a passive device, the signal suffers from insertion loss when passed through the filter, thus resulting in loss of SNR. This is further exacerbated by the fact that in practice, the out-of-band rejection of the spike train filter is finite, which results in further loss of SNR. It is possible to reduce the impact of this SNR loss at the circuit level by improving impedance matching and the isolation between input and output ports. We can also compensate for the SNR loss by averaging the channel measurements across multiple OFDM symbols.
- *Line-of-sight*: Similar to many localization systems, *ISLA* assumes the availability of line-of-sight (LoS) paths to the base stations which might not hold under occlusion. This, however, can be addressed by potentially selecting a subset of base stations with LoS paths using similar techniques demonstrated in [21]. With the dense deployment of 5G base stations, we expect a significant subset of base stations to have LoS path to the node.
- *Fast Mobility*: The current design of *ISLA* is not suitable for highly dynamic applications with fast mobility such as tracking cars. This is because the localization algorithm must receive wideband 5G packets from 4 or more base stations before it can self-localize.
- *Multiple Providers*: *ISLA* can benefit from capturing signals from multiple different providers since the IoT node does not need to associate with the base stations. However, different providers operate in different frequency bands which would require different spike-train filters. This could potentially be addressed by having multiple filters and switching between them similar to our design in sec. 9.

Acknowledgements: We thank our shepherd, Vyas Sekar, and the anonymous reviewers for their feedback and comments. We also thank Steffen Link for his help with fabricating the hardware for this project. This work is funded in part by NSF award numbers: 1750725 and 1824320.

References

[1] Cell Mapper cell tower locations. https://www.cellmapper.net. Accessed: Mon, Sep 13, 2021.

[2] 3GPP. Study on narrow-band internet of things (NB-IoT) / enhanced machine type communication (eMTC) support for non-terrestrial networks (NTN). Technical Report (TR) 36.763, 3rd Generation Partnership Project (3GPP), 06 2021.

[3] Godfrey Anuga Akpakwu, Bruno J Silva, Gerhard P Hancke, and Adnan M Abu-Mahfouz. A survey on 5g networks for the internet of things: Communication technologies and challenges. *IEEE access*, 6:3619–3647, 2017.

[4] Heba Aly and Moustafa Youssef. Dejavu: an accurate energy-efficient outdoor localization system. In *Proceedings of the 21st ACM SIGSPATIAL International Conference on Advances in Geographic Information Systems*, pages 154–163, 2013.

[5] Atul Bansal, Akshay Gadre, Vaibhav Singh, Anthony Rowe, Bob Iannucci, and Swarun Kumar. Owll: Accurate lora localization using the tv whitespaces. In *Proceedings of the 20th International Conference on Information Processing in Sensor Networks (co-located with CPS-IoT Week 2021)*, pages 148–162, 2021.

[6] Sujittra Boonsriwai and Anya Apavatjrut. Indoor wifi localization on mobile devices. In *2013 10th International Conference on Electrical Engineering/Electronics, Computer, Telecommunications and Information Technology*, pages 1–5. IEEE, 2013.

[7] Mathieu Bouet and Aldri L Dos Santos. Rfid tags: Positioning principles and localization techniques. In *2008 1st IFIP Wireless Days*, pages 1–5. IEEE, 2008.

[8] Stephen Boyd, Stephen P Boyd, and Lieven Vandenberghe. *Convex optimization*. Cambridge university press, 2004.

[9] Rizanne Elbakly and Moustafa Youssef. Crescendo: An infrastructure-free ubiquitous cellular network-based localization system. In *2019 IEEE Wireless Communications and Networking Conference (WCNC)*, pages 1–6. IEEE, 2019.

[10] Sinan Gezici and Zafer Sahinoglu. Uwb geolocation techniques for ieee 802.15.4a personal area networks. *MERL Technical report*, 2004.

[11] Songbin Gong, Yong-Ha Song, Tomas Manzaneque, Ruochen Lu, Yansong Yang, and Ali Kourani. Lithium niobate mems devices and subsystems for radio frequency signal processing. In *2017 IEEE 60th International Midwest Symposium on Circuits and Systems (MWSCAS)*, pages 45–48. IEEE, 2017.

[12] Junfeng Guan, Jitian Zhang, Ruochen Lu, Hyungjoo Seo, Jin Zhou, Songbin Gong, and Haitham Hassanieh. Efficient wideband spectrum sensing using MEMS acoustic resonators. In *18th USENIX Symposium on Networked Systems Design and Implementation (NSDI 21)*, pages 809–825. USENIX Association, April 2021.

[13] Fredrik Gustafsson and Fredrik Gunnarsson. Mobile positioning using wireless networks: possibilities and fundamental limitations based on available wireless network measurements. *IEEE Signal processing magazine*, 22(4):41–53, 2005.

[14] Ismail Guvenc and Chia-Chin Chong. A survey on toa based wireless localization and nlos mitigation techniques. *IEEE Communications Surveys & Tutorials*, 11(3):107–124, 2009.

[15] Yixue Hao, Min Chen, Long Hu, Jeungeun Song, Mojca Volk, and Iztok Humar. Wireless fractal ultra-dense cellular networks. *Sensors*, 17(4):841, 2017.

[16] Haitham Hassanieh, Lixin Shi, Omid Abari, Ezzeldin Hamed, and Dina Katabi. Ghz-wide sensing and decoding using the sparse fourier transform. In *IEEE INFOCOM 2014 - IEEE Conference on Computer Communications*, pages 2256–2264, 2014.

[17] Mohamed Ibrahim and Moustafa Youssef. Cellsense: An accurate energy-efficient gsm positioning system. *IEEE Transactions on Vehicular Technology*, 61(1):286–296, 2011.

[18] Mohamed Ibrahim and Moustafa Youssef. A hidden markov model for localization using low-end gsm cell phones. In *2011 IEEE International Conference on Communications (ICC)*, pages 1–5. IEEE, 2011.

[19] Vikram Iyer, Rajalakshmi Nandakumar, Anran Wang, Sawyer B. Fuller, and Shyamnath Gollakota. Living iot: A flying wireless platform on live insects. In *The 25th Annual International Conference on Mobile Computing and Networking*, MobiCom '19, 2019.

[20] Michio Kadota, Shuji Tanaka, Yasuhiro Kuratani, and Tetsuya Kimura. Ultrawide band ladder filter using SH0 plate wave in thin LiNbO3 plate and its application. In *2014 IEEE International Ultrasonics Symposium*, pages 2031–2034, 2014.

[21] Manikanta Kotaru, Kiran Joshi, Dinesh Bharadia, and Sachin Katti. Spotfi: Decimeter level localization using wifi. In *Proceedings of the 2015 ACM Conference on*

Special Interest Group on Data Communication, pages 269–282, 2015.

[22] Somansh Kumar and Ashish Jasuja. Air quality monitoring system based on IoT using raspberry pi. In *2017 International Conference on Computing, Communication and Automation (ICCCA)*, pages 1341–1346. IEEE, 2017.

[23] Ruochen Lu, Tomás Manzaneque, Yansong Yang, Jin Zhou, Haitham Hassanieh, and Songbin Gong. Rf filters with periodic passbands for sparse fourier transform-based spectrum sensing. *Journal of Microelectromechanical Systems*, 27(5):931–944, 2018.

[24] E Manavalan and K Jayakrishna. A review of internet of things (IoT) embedded sustainable supply chain for industry 4.0 requirements. *Computers & Industrial Engineering*, 127:925–953, 2019.

[25] Andreas Marcaletti, Maurizio Rea, Domenico Giustiniano, Vincent Lenders, and Aymen Fakhreddine. Filtering noisy 802.11 time-of-flight ranging measurements. In *Proceedings of the 10th ACM International on Conference on emerging Networking Experiments and Technologies*, pages 13–20, 2014.

[26] Saman Naderiparizi, Yi Zhao, James Youngquist, Alanson P Sample, and Joshua R Smith. Self-localizing battery-free cameras. In *Proceedings of the 2015 ACM International Joint Conference on Pervasive and Ubiquitous Computing*, pages 445–449, 2015.

[27] Rajalakshmi Nandakumar, Vikram Iyer, and Shyamnath Gollakota. 3d localization for sub-centimeter sized devices. In *Proceedings of the 16th ACM Conference on Embedded Networked Sensor Systems*, pages 108–119, 2018.

[28] Aymen Omri, Mohammed Shaqfeh, Abdelmohsen Ali, and Hussein Alnuweiri. Synchronization procedure in 5g nr systems. *IEEE Access*, 7:41286–41295, 2019.

[29] Jeongyeup Paek, Kyu-Han Kim, Jatinder P Singh, and Ramesh Govindan. Energy-efficient positioning for smartphones using cell-id sequence matching. In *Proceedings of the 9th international conference on Mobile systems, applications, and services*, pages 293–306, 2011.

[30] Joan Palacios, Guillermo Bielsa, Paolo Casari, and Joerg Widmer. Communication-driven localization and mapping for millimeter wave networks. In *IEEE INFOCOM 2018-IEEE Conference on Computer Communications*, pages 2402–2410. IEEE, 2018.

[31] Joan Palacios, Paolo Casari, and Joerg Widmer. Jade: Zero-knowledge device localization and environment mapping for millimeter wave systems. In *IEEE INFOCOM 2017-IEEE Conference on Computer Communications*, pages 1–9. IEEE, 2017.

[32] Anshul Rai, Krishna Kant Chintalapudi, Venkata N Padmanabhan, and Rijurekha Sen. Zee: Zero-effort crowdsourcing for indoor localization. In *Proceedings of the 18th annual international conference on Mobile computing and networking*, pages 293–304, 2012.

[33] Hamada Rizk, Ahmed Shokry, and Moustafa Youssef. Effectiveness of data augmentation in cellular-based localization using deep learning. In *2019 IEEE Wireless Communications and Networking Conference (WCNC)*, pages 1–6. IEEE, 2019.

[34] Hazem Sallouha, Alessandro Chiumento, and Sofie Pollin. Localization in long-range ultra narrow band IoT networks using rssi. In *2017 IEEE International Conference on Communications (ICC)*, pages 1–6. IEEE, 2017.

[35] Ahmed Shokry, Marwan Torki, and Moustafa Youssef. Deeploc: a ubiquitous accurate and low-overhead outdoor cellular localization system. In *Proceedings of the 26th ACM SIGSPATIAL International Conference on Advances in Geographic Information Systems*, pages 339–348, 2018.

[36] Y. Song and S. Gong. Wideband spurious-free lithium niobate rf-mems filters. *Journal of Microelectromechanical Systems*, 26(4):820–828, 2017.

[37] Parvathanathan Subrahmanya and Amir Farajidana. 5g and beyond: Physical layer guiding principles and realization. *Journal of the Indian Institute of Science*, 100:263–279, 2020.

[38] Adam Thierer and Andrea Castillo. Projecting the growth and economic impact of the internet of things. *George Mason University, Mercatus Center, June*, 15, 2015.

[39] Deepak Vasisht, Zerina Kapetanovic, Jongho Won, Xinxin Jin, Ranveer Chandra, Sudipta Sinha, Ashish Kapoor, Madhusudhan Sudarshan, and Sean Stratman. Farmbeats: An iot platform for data-driven agriculture. In *14th USENIX Symposium on Networked Systems Design and Implementation (NSDI 17)*, pages 515–529, 2017.

[40] Deepak Vasisht, Swarun Kumar, and Dina Katabi. Decimeter-level localization with a single wifi access point. In *13th USENIX Symposium on Networked Systems Design and Implementation (NSDI 16)*, pages 165–178, 2016.

[41] Jue Wang and Dina Katabi. Dude, where's my card? rfid positioning that works with multipath and non-line of sight. In *Proceedings of the ACM SIGCOMM 2013 conference on SIGCOMM*, pages 51–62, 2013.

[42] Fuxi Wen, Henk Wymeersch, Bile Peng, Wee Peng Tay, Hing Cheung So, and Diange Yang. A survey on 5g massive mimo localization. *Digital Signal Processing*, 94:21–28, 2019.

[43] Yaxiong Xie, Jie Xiong, Mo Li, and Kyle Jamieson. md-track: Leveraging multi-dimensionality for passive indoor wi-fi tracking. In *The 25th Annual International Conference on Mobile Computing and Networking*, pages 1–16, 2019.

[44] Jie Xiong and Kyle Jamieson. Arraytrack: A fine-grained indoor location system. In *10th USENIX Symposium on Networked Systems Design and Implementation (NSDI 13)*, pages 71–84, 2013.

[45] Jie Xiong, Karthikeyan Sundaresan, and Kyle Jamieson. Tonetrack: Leveraging frequency-agile radios for time-based indoor wireless localization. In *Proceedings of the 21st Annual International Conference on Mobile Computing and Networking*, pages 537–549, 2015.

[46] Chouchang Yang and Huai-Rong Shao. Wifi-based indoor positioning. *IEEE Communications Magazine*, 53(3):150–157, 2015.

[47] Chaoyun Zhang, Paul Patras, and Hamed Haddadi. Deep learning in mobile and wireless networking: A survey. *IEEE Communications surveys & tutorials*, 21(3):2224–2287, 2019.

[48] C. Zuo, N. Sinha, and G. Piazza. Very high frequency channel-select mems filters based on self-coupled piezoelectric AlN contour-mode resonators. *Sensors and Actuators A: Physical*, 160(1):132 – 140, 2010.

A Proofs

Here we re-state the lemmas and provide proofs.

Lemma 5.1 *For a sub-sampling factor P and N OFDM subcarriers, the complex valued scaling factors for each subcarrier will be preserved upon aliasing if $N = z \times P$, for some integer z, given the aliasing results in no collisions.*

Proof of lemma 5.1: Assume that $x[n]$ is a discrete signal from 0 to $N-1$, and we are sub-sampling (or *decimating*) it by a factor of P, meaning $y[n] = X[n \times P]$ for some integer P. Then the Discrete Fourier Transform of $y[n]$, denoted by $\hat{Y}[k]$ is

$$\begin{aligned}\hat{Y}[k] &= \sum_{n=0}^{\lfloor N/P \rfloor -1} x[nP] e^{-j2\frac{2\pi}{\lfloor N/P \rfloor}kn} \\ &= \frac{1}{P}\sum_{n=0}^{N-1} x[n] \sum_{m=0}^{P-1} e^{j\frac{2\pi}{P}mn} e^{-j2\frac{2\pi}{\lfloor N/P \rfloor}\frac{kn}{P}} \\ &= \frac{1}{P}\sum_{m=0}^{P-1}\Big(\sum_{n=0}^{N-1} x[n] e^{-j(\frac{2\pi}{N}n)(k\frac{N/P}{\lfloor N/P \rfloor}-\frac{N}{P}m)}\Big).\end{aligned}$$

Now if P divides N, in other words $N = Pz$ for some integer z, the above simplifies to

$$\begin{aligned}\hat{Y}[k] &= \frac{1}{P}\sum_{m=0}^{P-1}\Big(\sum_{n=0}^{N-1} x[n] e^{-j(\frac{2\pi}{N}n)(k-zm)}\Big) \\ &= \frac{1}{P}\sum_{m=0}^{P-1}\hat{X}[k-zm],\end{aligned}$$

where $\hat{X}$ is the DFT of $x[n]$. This proves that, as long as there is no collision, meaning that there is at most one index m in the above equation for which $\hat{X}[k-zm] \neq 0$, then the complex values of $\hat{X}[k]$ will be fully preserved upon sub-sampling. This proves the lemma.

We also point out that if P does not divide N, then the complex values are *not* preserved. Specifically, if N/P is not a proper integer, $\hat{Y}[k]$ will be in terms of $\hat{X}[k\frac{N/P}{\lfloor N/P \rfloor} - \frac{N}{P}m]$ where inside the argument, $k\frac{N/P}{\lfloor N/P \rfloor} - \frac{N}{P}m$, is not necessarily an integer. As a result, the original information of $\hat{X}[k]$ is never repeated in any of the $\hat{Y}$ indices. In fact, $\hat{Y}$ would closely relate to an interpolated version of $\hat{X}$ with the Dirichlet kernel.

Lemma 5.2 *Consider an OFDM symbol with N frequency subcarriers, indexed as $\{f_{\frac{-N}{2}}, \ldots, 0, \ldots, f_{\frac{N}{2}-1}\}$ with inter-frequency spacing of Δf, and a narrowband receiver that subsamples by $P\times$. If P^2 divides N, then the ideal filter parameters that meet all three requirements are: (1) $f_M^0 = f_{\frac{-N}{2}}$, (2) $\left(\frac{N}{P^2}-1\right)\times\Delta f < \Delta S < \frac{N}{P^2}\times\Delta f$, and (3) $\Delta F = \frac{N}{P}(1+\frac{1}{P})\times\Delta f$.*

Proof of Lemma 5.2: First, we show that no two frequencies collide after aliasing. Let $q = \frac{N}{P}$, and assume that two frequencies f_α and f_β collide. Let f_α be k-th subcarrier (for $0 \leq k < P$) covered at the i-th passband ($0 \leq i < \left\lceil \frac{\Delta S}{\Delta f} \right\rceil$), and let f_β have k' and i' as corresponding indices. To collide after aliasing, $f_\alpha - f_\beta = (k-k')\Delta F + (i-i')\Delta f$ must be an integer multiple of $q\Delta f$. However, $|k-k'| \leq P-1$ and $|i-i'| < \frac{N}{P^2}$. Thus $\frac{|f_\alpha - f_\beta|}{\Delta f} < (\frac{P-1}{P}+\frac{1}{P})q = q$, meaning we must have $f_\alpha - f_\beta = 0$, proving the first design requirement. Second, we note that P passbands that do not overlap (since $\Delta S < \Delta F$), and each passband covers exactly $\frac{N}{P^2}$ subcarriers. We therefore have

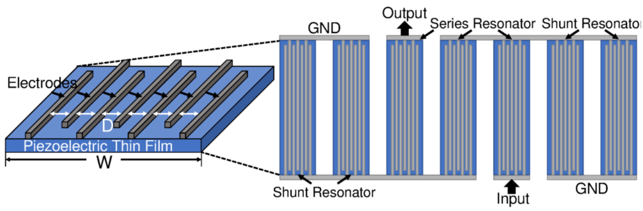

Figure 12: MEMS Spike-Train Filter Architecture

a total of $P \times \frac{N}{P^2} = q$ subcarriers that, as we just showed, do not overlap after aliasing. Therefore, after aliasing, each of the q subcarriers is covered exactly once, ensuring the second design requirement. Finally, we note that the smallest bin index is covered by the filter is $\min f_M = \frac{-N}{2}$, and the largest bin index is the last bin of the last passband, whose index can be computed as follows:

$$\begin{aligned}\max f_M &= \frac{-N}{2} + (P-1) \times \Delta F + \left\lceil \frac{\Delta S}{\Delta f} \right\rceil - 1 \\ &= \frac{-N}{2} + (P-1) \times \frac{N}{P}(1+\frac{1}{P}) + (\frac{N}{P^2}) - 1 \\ &= -\frac{N}{2} + N - 1 = \frac{N}{2} - 1.\end{aligned}$$

Thus, the entire bandwidth (including $f_{\frac{-N}{2}}$ and $f_{\frac{N}{2}-1}$) is covered, ensuring the last design requirement.

B MEMS Spike-Train Filter

Spike-Train Filter Implementation: Following Lemma 5.2, we can derive the desired frequency response of the spike-train filter, and design MEMS resonators topology accordingly. For example, in our experiment, we used a 100 MHz 5G-like OFDM waveform with N=2048 subcarriers and a subcarrier spacing $\Delta f = 49\ kHz$, and we down-sample the filtered waveform by a factor of P=16. According to Lemma 5.2, the desired filter should 16 spikes with a spike spacing of 6.64 MHz spanning the 100 MHz bandwidth, and each spike should have a width around 400 kHz.

We can design a spike-train filter leveraging the periodic resonance frequencies of a type of MEMS acoustic resonators that is commonly referred to as a LOBAR (Lateral Overtone Bulk Acoustic Resonator). As shown in Fig. 12, the LOBAR resonator consists of 12 electrodes on the top of a thin film made of the piezoelectric material $LiNbO_3$. And we combine seven resonators in a ladder filter topology [20] to build a filter circuit. As a result, the LOBAR resonator architecture determines the spike frequencies, whereas the slight difference between different resonators determines the width of the spikes. For simplicity, here we only focus on these two key parameters of the spike-train filter response, since they are restricted by our channel recovery algorithm as described in Sec. 5. More details on the MEMS spike-train filter design can be found in [23].

(1) The width of the film: the spacing between spikes Δf is determined by the width of the thin film W as $\Delta f = v/W$, where v is the acoustic velocity in the piezoelectric material, which is $\sim 4\ km/s$ in our design. Therefore, to achieve the 6.6 MHz spike spacing, we design the film width W to be $\sim 660\ \mu m$.

(2) The film width difference between different shunt and series resonators: the spike width ΔF of the spike-train filter equals to the resonant frequency difference between shunt and series resonators in the ladder filter, which is determined by the difference ΔW between shunt and series resonators: $\Delta F = fc\frac{\Delta W}{W}$. We design with piezoelectric film width to be 660 μm for series resonators and 660.26 μm for shunt resonators, which leads to $\Delta W = 0.26\mu m$, so that the widths of the spikes are around 400 kHz.

C Updated Objective Function to Account for Residual CFO

ISLA captures the narrowband channel and wideband channel from different subframes. Thus, there is going to be an additional phase accumulation between the two measurements due to residual CFO. To address this, we slightly modify Eq.6 where we split the objective function into two separate L-2 norm minimizations, with the first term containing only the wideband channel h'_M, and the second term containing only the narrowband channel h'_{NB}. This objective function is given below:

$$\begin{aligned}\{\tau_l^*\}_{l=1}^{L} = \arg\min_{\tau_1,\ldots,\tau_L} \Big(&\|h'_M - V_M F_N \Psi (V_M F_N \Psi)^{\dagger} h'_M\|^2 \\ &+ \|h'_{NB} - V_{NB} F_N \Psi (V_{NB} F_N \Psi)^{\dagger} h'_{NB}\|^2 \Big) \quad (7) \\ s.t. \quad \tau_l \geq 0 \quad &\forall\, l \in \{1,2,\ldots,L\}\end{aligned}$$

The modified objective function is now invariant to phase offsets between the two channels, and *ISLA* can solve this updated optimization using the same technique described in Sec. 6.